A novel method to tailor the porous structure of KOH-activated biochar and its application in Capacitive Deionization and energy storage

Amir Mehdi Dehkhoda, Előd Gyenge, Naoko Ellis *

Department of Chemical and Biological Engineering, The University of British Columbia, 2360 East Mall, Vancouver, BC, Canada, V6T-1Z3

Abstract

This study reveals a novel method to tailor the micro- and meso-porous structures of activated biochar by exploiting the interaction between pre-carbonization drying conditions and carbonization temperature in KOH activation. Biochar samples were mixed with concentrated KOH and then dried under air or nitrogen for various periods of time (0 -280 h) followed by carbonization at 475, 675 or 875°C. It is confirmed that by manipulating drying conditions and carbonization temperatures, the KOH activated biochar can have a predominantly microporous, mesoporous or a combined (micro/meso) porous structure. The surface area, micropore and mesopore volumes tailored between: 488 to 2670 m^2 g^{-1}, 0.04 to 0.72 cm^3 g^{-1}, and 0.05 to 1.70 cm^3 g^{-1}, respectively. The mechanism of porosity development was investigated by FTIR analysis suggesting conversion of KOH to K_2CO_3 due to different drying conditions as a major role in tailoring the structure. The application of activated biochar with tailored porosity was investigated for Electric Double Layer adsorption of NaCl/NaOH to be employed in water treatment (capacitive deionization) or energy storage (supercapacitor) processes. The majorly microporous activated biochar (N_2-dried activated at 675°C) showed promising capacitances between 220-245 F g^{-1}. Addition of mesoporous structure resulted in capacitances between 182-

* Corresponding author: Tel: +1 (604)-822-1243; Fax: +1 (604)-822-6003
Email address: naoko.ellis@ubc.ca

240 F g^{-1} with significantly reduced electrode resistance and improved capacitive behaviour as evidenced by Impedance Spectroscopy and Galvanostatic Charge/Discharge tests.

Keywords: Biochar; tailored porosity; Capacitive Deionization; supercapacitor; pre-carbonization drying; Chemical activation.

1. Introduction[1]

The worldwide demand for Activated Carbon (AC) is rising rapidly with a 10 % increase per year due to diverse applications ranging from pollution abatement to energy storage [1]. Chemical activation is one of the well-known processes to produce AC in which carbonaceous precursor is impregnated with chemical reagent and carbonized [2–8]. A large number of studies in the literature focused on the correlation between porosity development and activation process parameters including: activating reagent type [6,9]; mass ratio of activating reagent to substrate [5,7,10,11]; carbonization temperature [5,7,8,12]; flow rate of inert gas during carbonization [5,10,11,13]; carbonization time [5,14]; method of mixing [7,10]; and, washing step [11]. Even though the majority of reports have investigated different chemical activation parameters, the sample drying process prior to carbonization (i.e., a key step in all chemical activation processes) has not been investigated in detail. Drying conditions prior to carbonization affected the porosity development due to the potential conversion of activating reagents (e.g., KOH and NaOH) to their corresponding carbonates (i.e., K_2CO_3 and Na_2CO_3) in the presence of CO_2 in the air-dried [4,10]. According to the literature, chemical activation using KOH produced high surface area

[1] List of abbreviations:

- B-KOH-SD/LD/LLD-15h/140h/280h-Air/N_2: Impregnated biochar and KOH without carbonization at specific drying lengths (i.e., SD: 15 h, LD:140 h, and LLD:280 h) and atmosphere (i.e., Air or Nitrogen)
- B475/675/875-SD/LD/LLD-15h/140h/280h-Air/N_2: Carbonized biochar at 475, 675, or 875^{0}C with specific pre- carbonization drying lengths (i.e., SD: 15 h, LD:140 h, and LLD:280 h) and atmosphere (i.e., Air or Nitrogen)

ACs with mostly microporous structure [5–7,13]; while, K_2CO_3 produced ACs with both micro- and meso-porosity depending on the carbonization temperature [15–17]. Thus, further investigation of the different drying conditions on the conversion of KOH to K_2CO_3, including the presence or absence of CO_2 in the drying atmosphere (i.e., drying under air vs. N_2), and its role in tailoring the porosity at specific temperatures are warranted. Modification of drying conditions could be potentially an easy and low-cost process for tailoring the AC porous structure comparing to other methods such as Chemical Vapor Deposition (CVD) and silica templates [18,19].

Producing AC from waste and by-products gained attention since availability of low-cost precursors is necessary for the economic feasibility of large scale AC production [5,20,21]. In this work, biochar is used as a renewable and low-cost precursor for AC production. Biochar is a by-product of the pyrolysis process converting biomass into valuable products such as chemicals and energy [22–24]. Using biochar as a valued-added AC broadens its application as a renewable material in different processes also increasing the product utilization of pyrolysis process. The major market for biochar is currently soil conditioning; however, further applications in carbon sequestration and water remediation are reported in the literature [22,25,26]. Biochar has shown promising results in the removal of organic and inorganic contaminations (e.g., Cu^{2+}, Zn^{2+}, and Pb^{2+} ions) from wastewater with adsorption capacities up to 300 mg g^{-1} [26]. In all of these applications, tailoring the porous structure of activated biochar to target specific ions is paramount for obtaining the desired adsorption capacity.

The goal of the present work is to investigate an easy-to-prepare method for tailoring the micro-/meso-porous structure of KOH-activated biochar by exploiting synergistic effects, overlooked thus far in the literature, between biochar drying conditions (air vs. N_2 and time), and

carbonization temperature (between 475 and 875°C). The mechanism responsible for the observed effects is studied to provide insights into the pore forming processes. Furthermore, the application of activated biochar with controllable porosity in an electric-induced adsorption based on Double Layer (EDL) phenomenon is studied. EDL is a reversible adsorption process sought as a promising method for desalination of wastewater (i.e., Capacitive Deionization, CDI) and storing energy (i.e., supercapacitor) [27–30]. Our group has recently studied biochar as an electrode for Electric Double Layer (EDL) applications [25]. The present work extends the investigations on the correlation between controlled porosity (via novel and modified KOH-activation method) and EDL performance of activated biochar electrodes. Development of novel material with tailored pore structure to yield promising electrodes for EDL-based application is emphasized in the literature [31,32]. Tailored activated biochar could introduce a new generation of low-cost and renewable electrodes with improved performance for EDL applications including desalination (CDI) and energy storage (supercapacitors).

2. Materials and methods

2.1 Material preparations

2.1.1 Chemical activation of biochar powder

The as-received biochar samples studied in this work were provided by Dynamotiv Energy Systems (fast pyrolysis of Spruce whitewood at 600°C). As previously reported by our group, the first step of activation was mixing of highly concentrated potassium hydroxide (7 mol L^{-1} using deionized water as mixing medium with 90 % purity KOH pellets, Sigma Aldrich) and biochar (sieved between 50-180 µm mesh size) with 3.5:1 mass ratio (KOH:biochar) followed by stirring for 2 h at room temperature (i.e., 20°C) [25]. Upon completion of the mixing step, the

resultant mixture was centrifuged at 16800 RCF for 5 min. Centrifuging the samples provided better separation compared to filtration since using filter papers led to shrinkage as a result of exposure to highly concentrated KOH solution and problematic separation. After centrifuging, the impregnated samples were dried at 115°C under two different atmospheres: air or nitrogen, respectively, at four different durations of 0, 15, 140, and 280 h. Air drying was done in a typical low-temperature laboratory oven, while drying under nitrogen was done in a tube furnace with 80 cm^3 min^{-1} flow of ultra-pure nitrogen. The longest drying time of 280 h was conducted to investigate the extent of drying effect, and not necessarily meant to be practical from large scale production perspective. The dried samples were further treated in a carbonization step using three different temperatures 475, 675 or 875°C (with 3°C min^{-1} heating rate) under 260 cm^3 min^{-1} nitrogen flow for 2 h carbonization (or dwell) time. Both the activated and non-activated samples were excessively washed with distilled water and 0.1 mol L^{-1} HCl until the wash water became pH neutral and dried in oven at 115°C overnight (Figure 1).

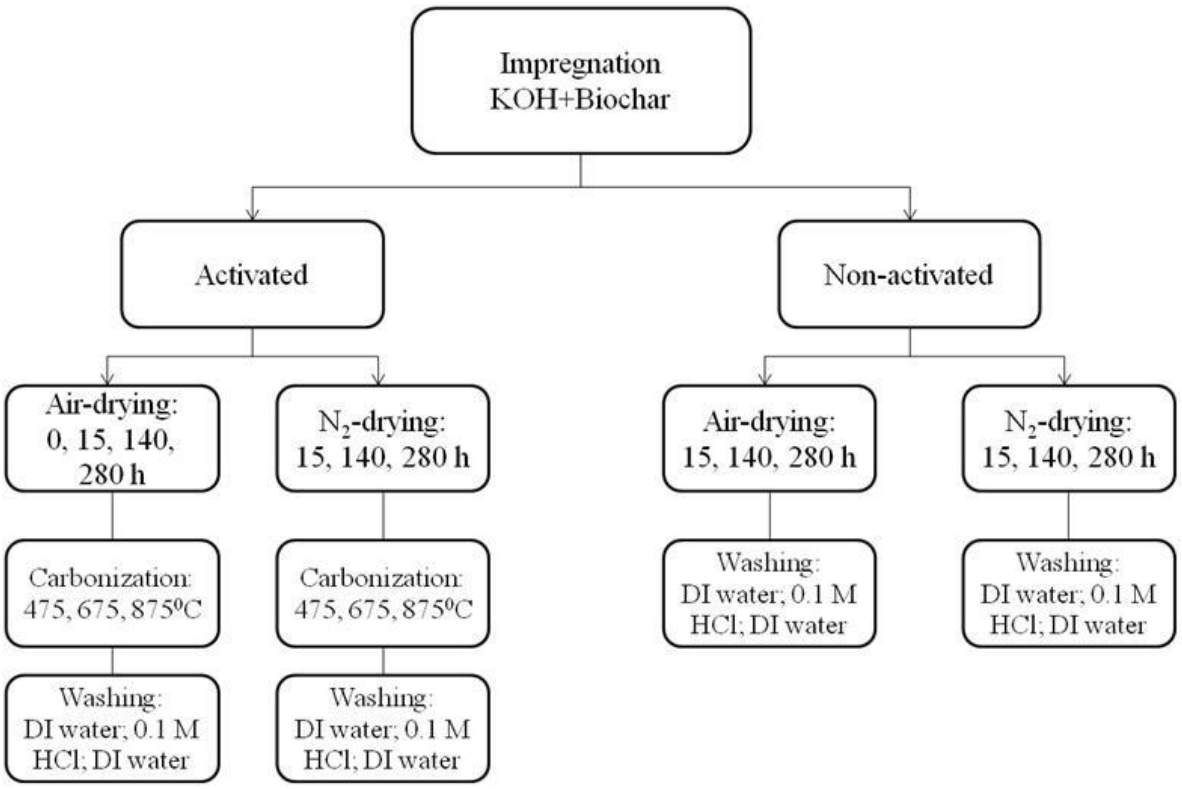

Figure 1. Schematic representation of activated biochar preparation.

For simplicity in referring to the prepared samples, from here on the notations B475, B675, and B875 are assigned to the activated biochar samples carbonized at 475, 675, and 875°C, respectively; while, the notation B-KOH was used for the non-activated samples. Furthermore, ND, SD, LD and LLD notations correspond to the drying duration of the samples: Not dried (ND), short dried (SD) for 15 h, long dried (LD) for 140 h and extra-long dried (LLD) for 280 h. Additionally, the drying gas (N_2 or air) followed the samples' name. For example: "B675-SD-15h-Air" refers to the activated biochar sample dried under air for 15 h (SD) and subsequently carbonized at 675°C. Further, the sample "B-KOH-LD-140h-N_2" refers to the sample dried under nitrogen for 140 h (LD) without carbonization.

2.1.2 Electrode preparation

Electrodes were fabricated by spraying the mixture of activated biochar powder (ground and sieved between 10-50 μm mesh size), iso-propanol (99.9 % assay Fisher Scientific), and Nafion® (mass fraction of 5 %, Sigma Aldrich) on Ni mesh (Monel® alloy, 150x150 mesh size, McMaster-Carr). The weight percentage of activated biochar to binder (i.e., Nafion®) was 95:5. Further electrode preparation details are described elsewhere [25]. The geometric area of electrodes was 8.54 ± 0.90 cm^2.

2.2 Characterization Methods

2.2.1 Physical and chemical characterization

The as-received biochar was sent to Microanalytical Services (Delta, BC) to be analyzed for elemental analysis, as shown in Table 1. Additionally, the ash content of the as-received biochar sample was characterized using LOI900 (Lost on Ignition at 900°C) method by Exova Labs in Surrey, BC, Canada. The majority of the ash consisted SiO_2 (60 %), Al_2O_3 and CaO (~8 % each).

Table 1. Elemental analysis and ash content of the as-received biochar

Sample	**C (%)**	**H (%)**	**N (%)**	**O (%)**	**Ash (%)**
As-received biochar	64.65	2.23	0.13	23.03	13.6

The porous structure of the samples was characterized by nitrogen adsorption/desorption at -196°C. The Brunauer-Emmet-Teller (BET), t-plot, and Barrett-Joyner-Halenda (BJH) methods were used to measure the total surface area, micropore volume, and mesopore volume of the prepared samples, respectively using a Micromeritics ASAP 2020 Accelerated Surface Area and Porosimetry Analyzer. The N_2 adsorption isotherms for all samples showed either type I or IV

according to IUPAC classification characteristic of microporous and mesoporous structures, respectively. To further analyze the micropore distribution of the selected samples, the Horvath Kawazoe (HK) method was employed using N_2 as adsorbing gas. Prior to BET, t-plot, and BJH analyses, 90 mg of each sample was vacuum degassed for 5 h at 120°C in the built-in degas port of the instrument. For HK analysis, 90 mg of sample underwent degassing for 8 hours at 300°C.

Surface chemical analysis of the various samples was studied via Fourier Transform Infra-Red (FTIR) spectroscopy using a Varian 3100 FT-IR Excalibur Series spectrometer with attenuated total reflectance: Pike MIRacle™ATR with ZnSe crystal. An aperture setting of 4 cm^{-1} with a wavenumber range of 4000-600 cm^{-1} and scan speed of 2.5 kHz was applied for spectra collection. For each sample, 64 scans were utilized to improve the signal-to-noise ratio.

The crystallographic structure of the samples was studied using X-ray Diffraction (XRD) analysis on a Bruker AXS D8 Advance X-ray Diffractometer (in Bragg-Brentano configuration) with a Lynxeye ID silicon strip detector. Cu radiation with Ni filter was generated at 40 kV and 40 mA. Custom-made sample holder with a shallow well was used for sample mounting.

To further investigate the structure, Transmission Electron Microscopy (TEM) images were taken using Tecnai G2 microscope at acceleration voltages of 20-200 kV. TEM grids were covered with 5 μL of the diluted powder samples in reagent grade ethanol (99.5 %, Extra Dry, Fisher Scientific) to provide more facile evaporation and product visibility during imaging.

2.2.2 Electrochemical characterization

Cyclic Voltammetry (CV), Galvanostatic Charge Discharge (GCD) and Impedance Spectroscopy (EIS) analyses were conducted in a three-electrode configuration at room temperature with Pt mesh as counter electrode and mercury/mercury oxide (Hg/HgO/KOH 0.1 mol L^{-1}) as reference

electrode. The electrolyte was composed of 0.1 mol L^{-1} NaCl in 0.1 mol L^{-1} NaOH to relate the results to the potential applicability of activated biochar electrodes for both water desalination through CDI (e.g., in chlor-alkali industry) and supercapacitor fabrication (e.g., using alkali electrolyte). CV analyses were conducted at potential scanning between 0.5-50 mV s^{-1} within -0.4 to +0.4 V potential window using 1100A Series Electrochemical Analyzer (CH Instrument, USA). GCD tests were performed by charging electrodes at constant current of 2 mA followed by sudden discharge at -2 mA for similar time intervals (20-150 s) using a Solartron 1470E potentiostat. The ohmic drop of electrodes (i.e., iR resistance) was measured by the amount of potential drop while changing the current from 2 to -2 mA in GCD analysis. The alternating current AC impedance spectroscopy was performed using Solartron 1470E and the spectrum was analyzed using Multistat® software. The AC potential amplitude was 10 mV and the frequency ranged between 10^{-2} to 10^{5} Hz.

Electrical conductivity of tailored activated biochar powders was measured via dry-cell Linear Sweep Voltammetry (LSV). About 20 mg of ground and sieved powders (10-50 μm mesh size) was dried in oven at 120°C for 2 h and placed between ultra conductive Cu plates (alloy 101, McMaster-Carr) with 2 mm distance. Constant potential sweep (20 mV s^{-1}) applied to the copper plates and potential was plotted against current. Ohmic resistance was then measured from the slope of the diagram and used for Electrical Conductivity (EC) measurement.

3. Results and Discussions

One of the working hypotheses is that the drying conditions prior to carbonization, such as drying gas (air vs. N_2), temperature and drying time can have a significant role on porous structure development through synergistic effects, an aspect largely neglected in the literature.

Regarding the drying gas, air drying of the KOH impregnated samples inherently exposes them to CO_2 and carbonate formation will occur (Equation 1).

$$4KOH+2CO_2 \Leftrightarrow 2K_2CO_3+2H_2O, \quad \Delta G^o = -141.07 \text{ kJ mol}^{-1} CO_2 \text{ at } 25°C \qquad (1)$$

Longer air drying time is expected to yield higher amount of K_2CO_3 and consequently it is hypothesized that different porous structures will be generated during the carbonization step. The conversion of KOH to K_2CO_3 under different drying conditions and its synergetic effect on tailoring the porosity at different carbonization temperatures are investigated in the following sections.

3.1 Effect of drying conditions on conversion of KOH to K_2CO_3 prior to carbonization

3.1.1 Surface chemistry analysis of impregnated biochar

First, the surface chemistry of air- and N_2-dried samples for different lengths of time was analyzed using FTIR.

Figure 2 shows the FTIR spectra of air-dried samples along with pure K_2CO_3. A broad peak around 3200 cm^{-1} in the B-KOH-ND and B-KOH-SD-15h-Air spectra is attributed to the presence of water which is absent in samples dried for 140 and 280 h. This broad peak at 3200 cm^{-1}might also overlapped the distinctive sharp peak around 3500 cm^{-1}, characteristic of the -OH group in KOH [33] (see Figure 3; KOH spectrum). Additionally, both B-KOH-LD-140h-Air and B-KOH-LLD-280h-Air showed similar peaks to the pure K_2CO_3 spectrum (Figure 2), most probably due to the conversion of KOH to K_2CO_3 during long drying times under air (i.e., 140 and 280 h, respectively). The spectra of air-dried samples compared with pure K_2CO_3 also reveal two additional peaks at 1560 and 760 cm^{-1} corresponding to the aromatic structure of biochar.

The former peak is attributed to the aromatic C-C bonding within the ring; while, the latter stands for the out-of-plane bonding of C-H bonds of aromatic and heteroatomic species [33,34].

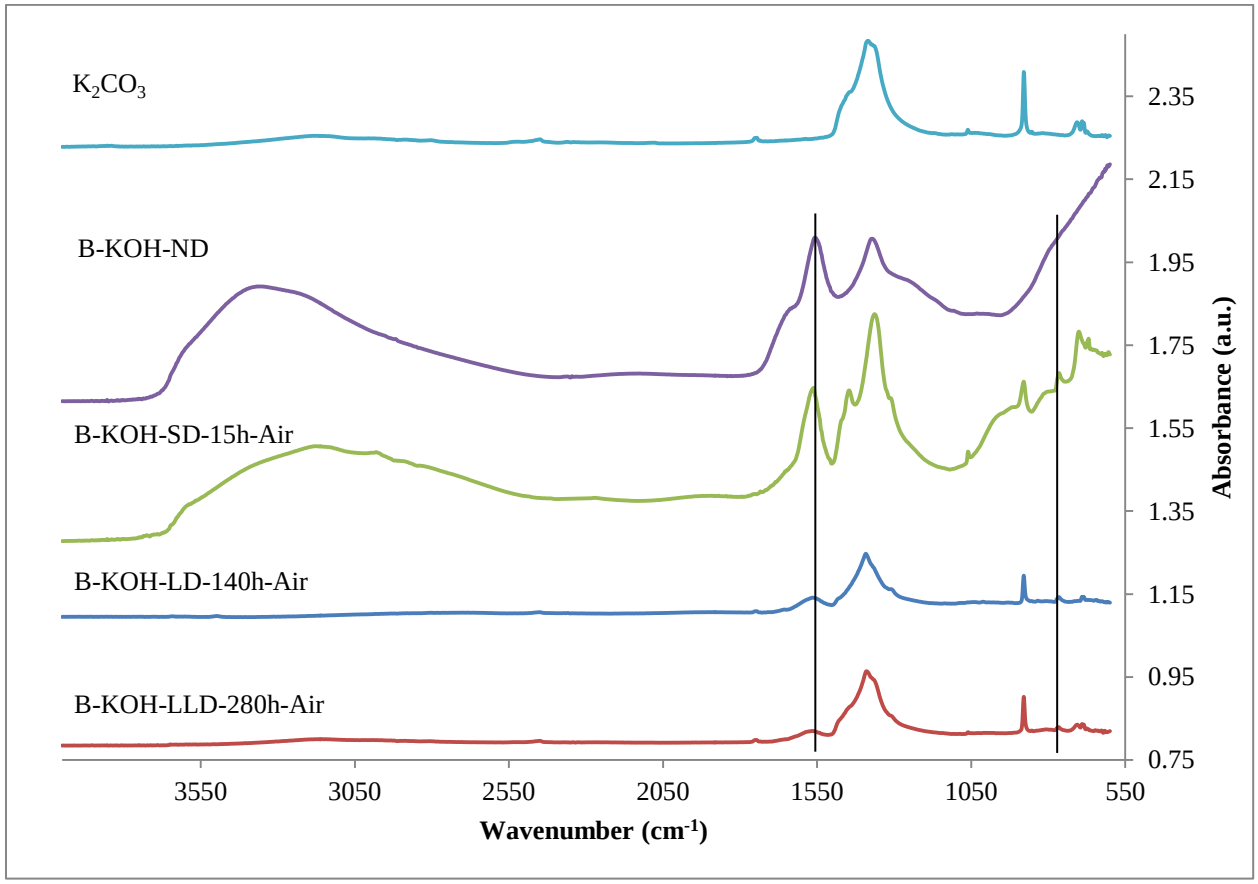

Figure 2. FTIR spectra of Air-dried samples compared with K_2CO_3.

To further investigate the effect of drying condition, samples dried under N_2 (i.e., for 15, 140, and 280 h) and analyzed using FTIR. As shown in Figure 3, a distinctive sharp peak at 3500 cm^{-1} along with broad peaks at 2700, 2450 and 1900 cm^{-1} can be observed for all N_2-dried samples similar to the pure KOH spectrum. However, comparing the spectra of air-dried samples suggested a trend of absence of peaks at 2700, 2450 and 1900 cm^{-1} as increasing the drying time (Figure 2). Hence, it is proposed that KOH is virtually absent in the air-dried samples. Additionally, comparing the FTIR spectra of B-KOH-SD-15h-Air and B-KOH-SD-15h-N_2

(Figures 2 and 3) reveals the absence of the broad peak around 3200 cm^{-1} (i.e., representative of the water in the sample) in B-KOH-SD-15h-N_2 sample. Since both samples were dried at the same temperature and time, the origin of the water present in the air-dried sample could be from the conversion of KOH to K_2CO_3 based on Equation (1). Hence, comparing Figures 2 and 3 suggest the conversion of KOH to K_2CO_3 under air and the preservation of KOH under N_2.

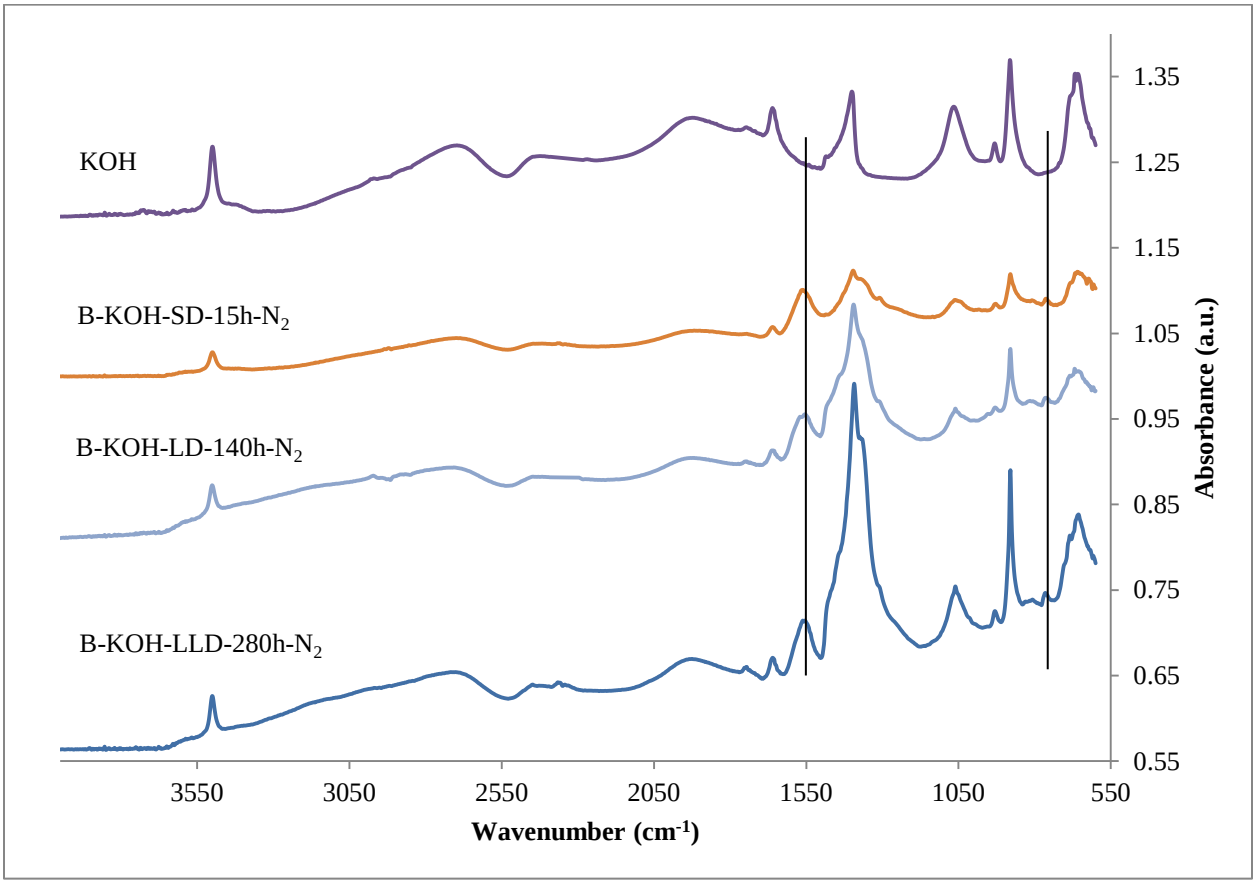

Figure 3. FTIR spectra of N_2-dried samples compared with KOH.

To further confirm the conversion of KOH to K_2CO_3, the B-KOH-LLD-280h-Air and B-KOH-LLD-280h-N_2 samples were analyzed via XRD spectroscopy (Figure 4). The XRD pattern showed peaks corresponding to the K_2CO_3 crystalline structure namely at 2θ= 13, 26, 29, 38, 48 and 51 ^{0} which were clearly absent for the B-KOH-LLD-280h-N_2 sample.

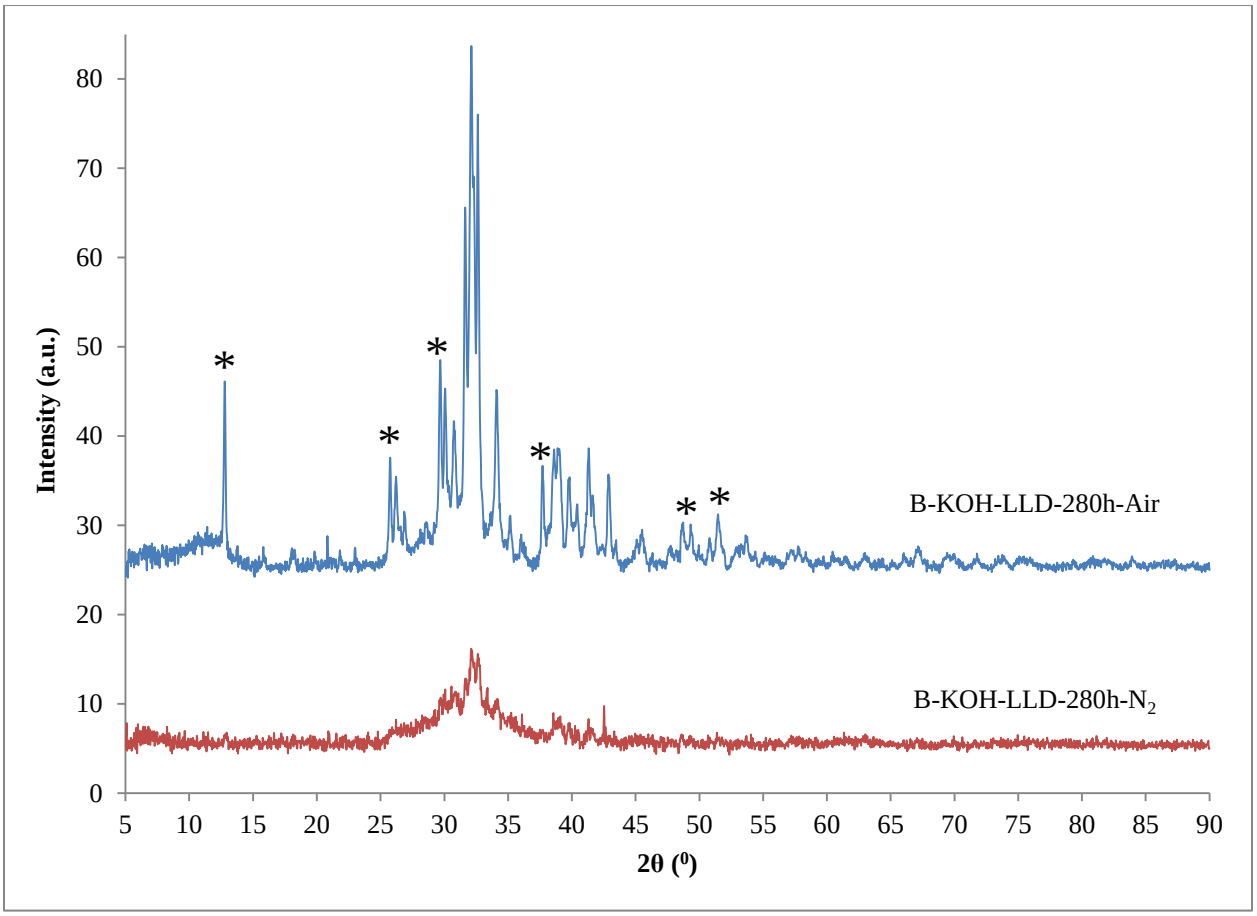

Figure 4. XRD pattern of B-KOH-LLD-280h-Air and B-KOH-LLD-N2 (starred peaks are indicative of K_2CO_3 from KOH crystalline structure).

3.1.2 Physical characteristics of air or nitrogen dried samples

The effect of drying conditions on the impregnated samples is expressed as drying percentage, i.e., defined as the percentage of water removed from the sample by drying compared to the initial (non-dried) sample mass. Results suggested virtually constant drying percentage between 54 – 58 % comparing air-dried and N_2-dried samples at different lengths. The air- or N_2 – dried samples were washed with distilled water and HCl (Section 2.1) and further analyzed via N_2 adsorption isotherms (at -196°C). The as-received biochar showed very small amount of BET surface area, i.e., 1.7 m^2 g^{-1}. The BET surface area and porosity of the air- and N_2-dried samples

(without carbonization) showed negligible increase compared to the as-received biochar, i.e., <1 $m^2 g^{-1}$, suggesting no structural development as a result of different drying conditions.

3.2. Tailoring the biochar porous structure: Synergy between drying conditions and different carbonization temperatures

The combined effects of drying conditions (i.e., under N_2 or air for 15, 140, and 280 h) and carbonization temperature (i.e., 450, 675, and 875°C) on tailoring the porous structure of activated biochar is investigated. There are different interpretations in the literature regarding the chemical activation mechanism of carbons. In general, activation with alkali metal hydroxides includes oxidation of carbon and reduction of hydroxide. It is commonly reported in the literature that chemically activated carbon with KOH has mostly microporous structure (i.e., >85 % of total pore volume) with high surface area (900-3000 $m^2 g^{-1}$) [5,13,35,36]. Lillo-Rodenas et al. measured Gibbs energies of their proposed reactions for chemical activation using alkali metal hydroxides [4]. According to the calculated standard Gibbs energies, the reaction of carbon with alkali-metal hydroxide (e.g., KOH) producing carbonate and hydrogen is the beginning of chemical activation process, i.e., Equation (2). This reaction is thermodynamically possible at temperatures around 475-530°C [4,36,37]. The produced metallic K is mobile within biochar matrix further contributing to pore enlargement through intercalation between the carbon sheets at >600°C [36,38,39].

$$6KOH + C \Leftrightarrow 2K + 2K_2CO_3 + 3H_2 \quad (2)$$

Chemical activation via K_2CO_3 has been also reported in the literature [12,15,17,40]. Reaction (3) was proposed by McKee at temperatures around 700°C for gasification of graphite where carbon is consumed by K_2CO_3 to produce CO [40]. The produced metallic K could further

develop porosity by intercalation through carbon sheets to enlarge the pores. Hayashi et al. reported K_2CO_3 as an effective chemical activation reagent with different porosity development behaviour at temperatures below or above 600°C [12,15]. At temperatures <600°C both micro- and meso-porosity were developed with the majority of the former structure due to the removal of tarry material within the pores. The surface area and mesopore volume increased considerably with activation temperature in the range of 700-900°C due to gasification of carbon generating additional porosity followed by intercalation of metallic K to enlarge the pores. Adinata et al. has made similar observation using K_2CO_3 at 600-1000°C [16]; noting, the highest mesopore volume and surface area were obtained at 800°C based on Equation (3).

$$K_2CO_3+2C \rightarrow 2K+3CO \quad (3)$$

Increasing the carbonization temperature >800°C would further change the mechanism of porosity development. Potassium carbonate is known to decompose >800°C resulting in potassium oxide and CO_2 as shown in Equation (4) [15,37]. These products can further develop the porosity based on two phenomena: (a) potassium oxide reacts with carbon to produce metallic K and CO which further contributing to the pore enlargement; and, (b) CO_2 oxidizes carbon to generate porosity as an activating reagent similar to physical activation mechanism. Equations (4) and (5) show the major reactions occurring >800°C.

$$K_2CO_3 \rightarrow K_2O+CO_2 \quad (4)$$

$$K_2O+C \rightarrow 2K+CO \quad (5)$$

Based on Equations (2)-(5), it can be deduced that K_2CO_3 and KOH both have important effects on developing the surface area and porosity of carbon at different activation temperatures. The

results presented in Section 3.1.1 suggested conversion of KOH to K_2CO_3 in air-dried samples specifically with long drying times (i.e., 140 and 280 h); while, KOH was preserved under N_2 at all drying times. Hence, it is speculated that the drying conditions can be used to tailor the structure of activated biochar at different temperatures as will be discussed in the following sections.

3.2.1 Effect of drying conditions at 475℃ carbonization temperature

Table 2 shows the effect of drying conditions on the surface area and porosity of the activated biochar at 475°C. The BET surface area and the micropore volume of air-dried samples showed decreasing trends with increasing drying time from 814 to 488 $m^2\ g^{-1}$ and 0.32 to 0.17 $cm^3\ g^{-1}$, respectively. However, prolonging drying under N_2 did not result in significant change of either surface area or micro/meso-pore volumes (i.e., <2 % drop in values). The surface area and porosity results of N_2-dried samples were also comparable to those of B475-ND (i.e., carbonization without drying). These results suggest that activated biochar samples with high micropore volume and surface area can be produced upon drying the samples under N_2 prior to carbonization at 475°C; while, drying samples under air prior to carbonization produced mixed micro- and meso-pore structure with reduced micropore volume and surface area.

Table 2. Surface area and porosity of activated biochar samples with different drying conditions and activation temperatures.

Sample	**BET surface area ($m^2\ g^{-1}$)**	**t-plot micropore volume ($cm^3\ g^{-1}$)**	**BJH mesopore volume ($cm^3\ g^{-1}$)**	**Average pore width[1] (nm)**	**CY[2] (%)**	**WY[3] (%)**
B475-ND	814	0.32	0.05	1.94	40	17
B475-SD-15h-Air	643	0.24	0.10	2.21	85	15
B475-LD-140h-Air	639	0.19	0.36	3.11	93	15
B475-LLD-280h-Air	488	0.17	0.14	2.41	94	13
B475-SD-15h-N_2	894	0.35	0.06	1.95	75	15
B475-LD-140h-N_2	868	0.34	0.06	1.95	83	12
B475-LLD-280h-N_2	841	0.33	0.07	2.01	94	15

B675-ND	1675	0.67	0.09	1.91	37	12
B675-SD-15h-Air	1317	0.54	0.22	2.20	87	12
B675-LD-140h-Air	876	0.33	0.20	2.31	91	13
B675-LLD-280h-Air	961	0.31	0.43	2.77	91	12
B675-SD-15h-N_2	1807	0.73	0.09	1.90	82	10
B675-LD-140h-N_2	1784	0.72	0.10	1.92	83	11
B675-LLD-280h-N_2	1695	0.69	0.12	1.95	80	11
B875-SD-15h-Air	2024	0.10	1.36	2.82	49	7.1
B875-LD-140h-Air	2079	0.18	1.70	3.43	62	7.5
B875-LLD-280h-Air	2046	0.22	1.33	2.90	49	9.5
B875-SD-15h-N_2	2247	0.08	1.41	2.76	37	5.5
B875-LD-140h-N_2	2673	0.04	1.64	2.70	40	9.3
B875-LLD-280h-N_2	2242	0.09	1.33	2.67	39	7

[1] Calculated based on BET method (4V/A)
[2] CY: Carbonization Yield = (mass of sample after carbonization) / (mass of sample before carbonization)
[3] WY: Washing Yield = (mass of sample after washing) / (mass of sample before washing)

3.2.2 Effect of drying conditions at 675℃ carbonization temperature

Increasing the carbonization temperature from 475 to 675°C has almost doubled both the surface area and micropore volume of the activated samples dried under either air or N_2, most probably due to the higher rates of Equations (2) and (3) (Table 2). Moreover, both air- and N_2-dried samples activated at 675°C showed similar trends of surface area and porosity change to those of analogous samples activated at 475°C: a trend of decreasing surface area (i.e., by 33 %) and micropore volume (i.e., by 39 %) with increasing the air drying time; and, comparable surface area with majority of microporosity for N_2-dried samples (i.e., <5 % difference) (Figure 5). These results could further confirm the preservation of KOH in N_2-dried samples leading in significantly higher surface area, micropore volume, and carbon burn-off (i.e., Carbonization Yield in Table 2) compared to air-dried samples.

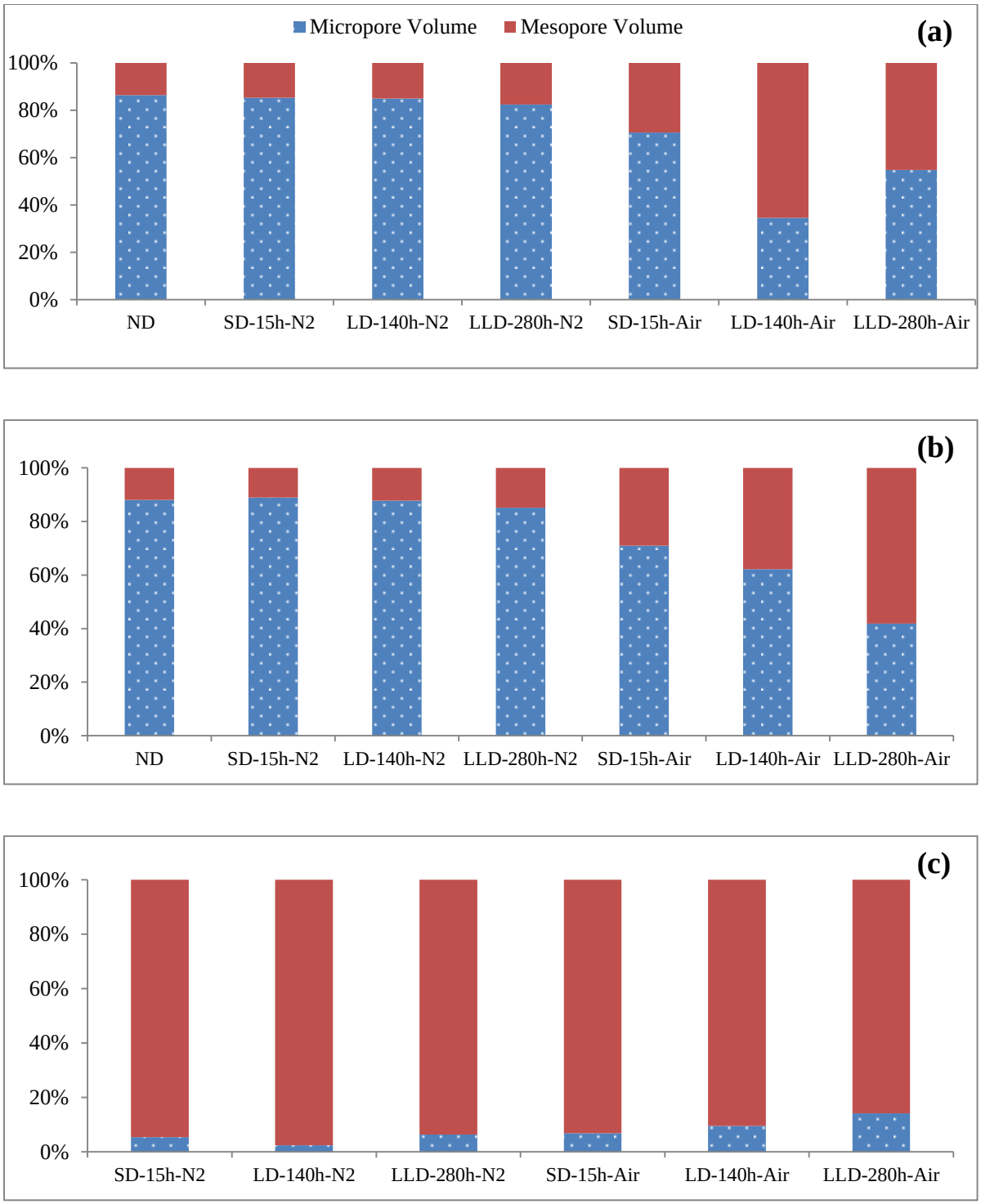

Figure 5. Micropore and mesopore distribution (i.e., Based on total pore volume calculated as the sum of BJH mesopore volume and t-plot micropore volume) of activated biochar samples: (a) B475; (b) B675; and, (c) B875 samples.

It is interesting to note that all air-dried samples activated at either 475 or 675°C showed higher mesopore volume (almost twice) comparing to the analogous N_2-dried samples resulting in activated biochar with both meso- and micro-pore structure.

3.2.3 Effect of drying conditions at 875℃ carbonization temperature

As shown in Table 2, increasing the carbonization temperature further to 875°C generated considerably higher surface area (i.e., >2000 $m^2 g^{-1}$) and mesopore volume (i.e., >1.5 $cm^3 g^{-1}$). Typically, high surface areas of chemically activated samples with KOH is attributed to their microporous structure [5,13,35,36]. However, the high surface area of air-dried and N_2-dried biochar samples activated at 875°C in the present study is mostly mesoporous, i.e., constituting >90 % of the total pore volume (Figure 5).

The mesopore volume of the B875 samples dried under N_2 and air was comparable with < 2 % difference (Table 2 and Figure 5). This is in contrary to the mesopore volume change of air- and N_2-dried samples activated at lower temperatures of 475 and 675°C (Table 2 and Figure 5). This difference may be due to the decomposition of K_2CO_3 during carbonization at 875°C vs. 475 and 675°C as previously shown in Equation 4. Therefore, conversion of KOH to K_2CO_3 (i.e., as a result of pre-carbonization drying) did not result in different mesoporosity of air-dried and N_2-dried samples activated at 875°C. Decomposition of K_2CO_3 at 875°C and its contribution to pore development of biochar samples via Equation (5) can be further confirmed through significantly smaller CY values of B875 samples compared to B475 and B675 (see Table 2).

For B875 samples with large mesopore volumes, the amount of micropore estimated via t-plot method might not be exact due to capillary condensation in the mesopores. Capillary condensation is the process in which pores are filled with condensed vapour of adsorbing gas

occurring at pressures lower than saturation vapor pressure [41]. To further investigate the micropore content, the B875 samples were analyzed via Horvath Kawazoe (HK) method specifically used to measure the micropore content and distribution [42–44]. The HK micropore volume of B875 samples were ranged between 0.65-0.85 $cm^3\ g^{-1}$. As a representative value, the HK micropore content of B875-SD-15h-Air sample was 0.65 $cm^3\ g^{-1}$ (with 0.79 nm median pore width) much higher than t-plot micropore presented in Table 2 (i.e., 0.10 $cm^3\ g^{-1}$); however, the majority of B875-SD-15h-Air structure has remained mesoporous (i.e., ~70 %) upon recalculation of total pore volume based on the HK micropore.

To further study the origin of mesoporous structure of B875 samples, Transmission Electron Microscopy (TEM) images were obtained. The TEM images of B875 samples were compared with those of B475 and B675 dried under either N_2 or air (Figures 6 and 7). B475 and B675 samples showed amorphous structure; while, the B875 samples (both N_2 and air dried) showed tube-like structures most probably responsible for the large mesopore volumes of these samples. These tube-like structures could be attributed to the excessive intercalation of mobile metallic K at 875°C (Equation 4) resulting in bending the carbon sheets. Further analysis of the tube-like structure of B875 samples is in progress in our group.

a)

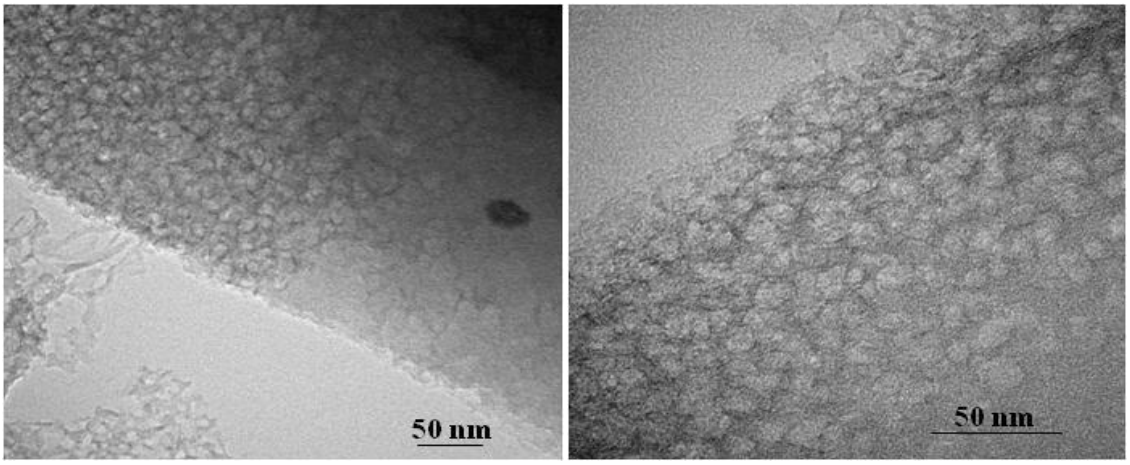

b)

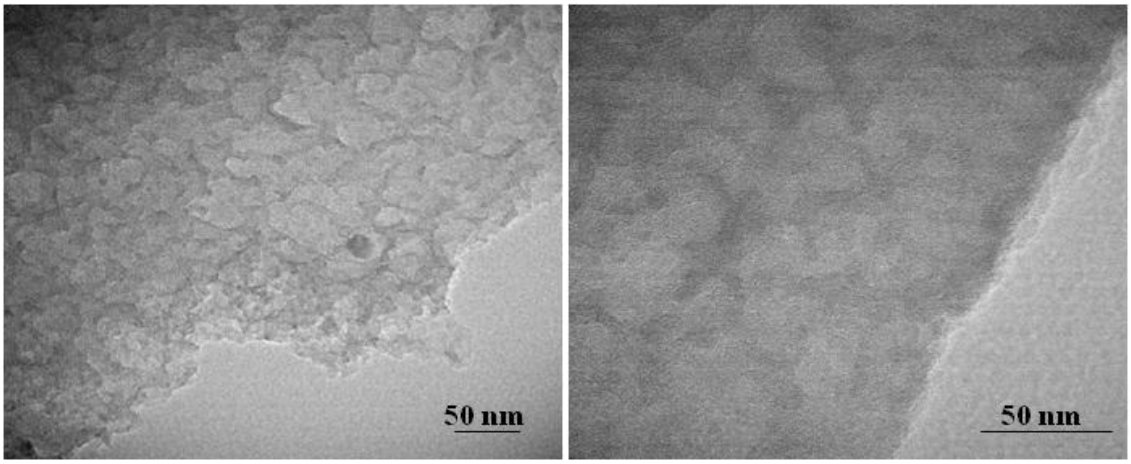

c)

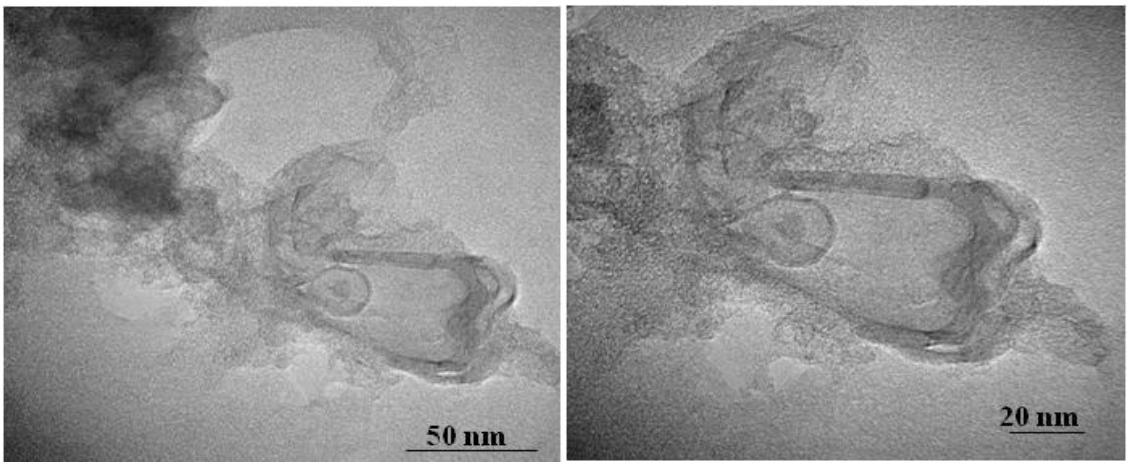

Figure 6. TEM images of: a) B475-LD-140h-Air; b) B675-LD-140h-Air; and, c) B875-LD-140h-Air.

a)

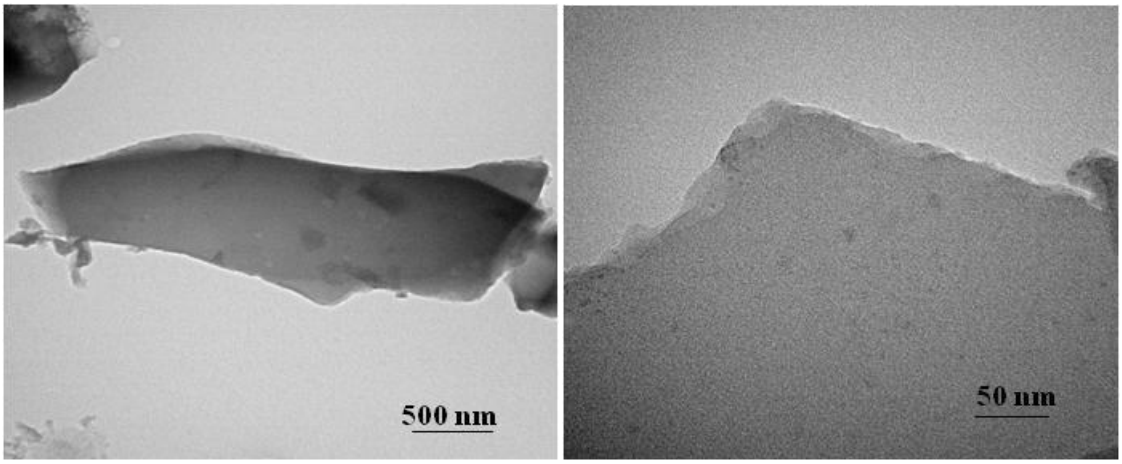

b)

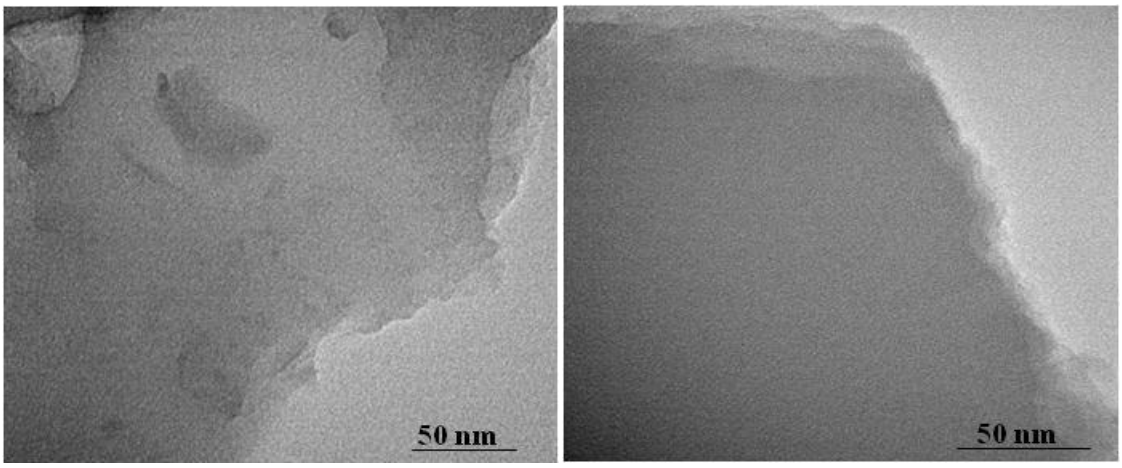

c)

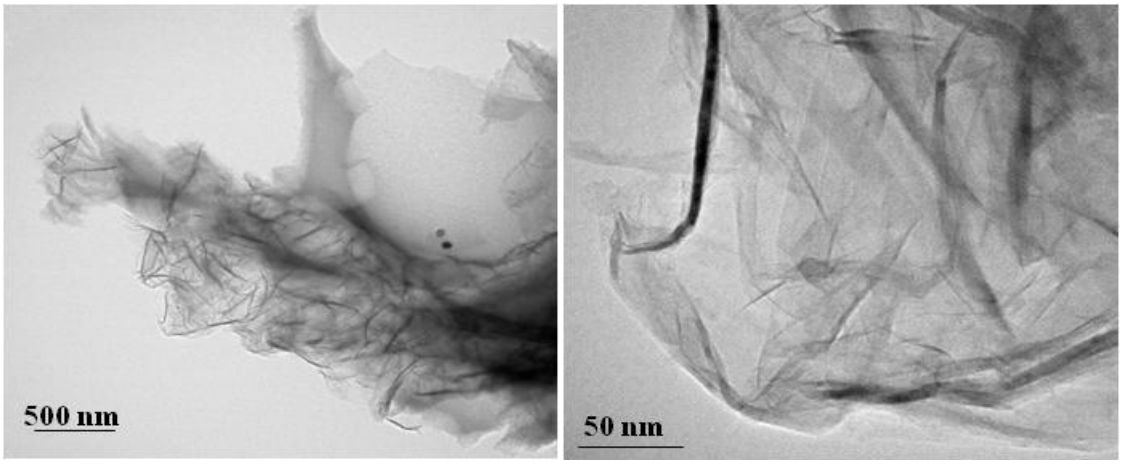

Figure 7. TEM images of: a) B475-LD-140h-N_2; b) B675-LD-140h-N_2; and, c) B875-LD-140h-N_2.

The significantly large mesoporous surface area of B875 samples, reported for the first time in this study, could be very advantageous for the employment of the activated biochar samples in applications requiring specific mesoporous structures such as catalyst supports in fuel cells and in the electric double layer capacitors (Section 3.3).

3.3. Application of tailored activated biochar in electric induced adsorption processes for desalination and energy storage

Tailored activated biochar was investigated for Electric Double Layer (EDL) adsorption applications, i.e., capacitive deionization (CDI) of NaCl in alkali solution, and supercapacitor fabrication. Three groups of electrodes were fabricated from selected activated biochar samples with tailored porosity: (a) majorly microporous (>85 % of the total pore volume), i.e., B675-SD-15h-N_2, B675-LD-140h-N_2 and B675-LLD-280h-N_2; (b) mixed microporous and mesoporous, i.e., B675-LD-140h-Air and B675-LLD-280h-Air (40-50 % of total pore volume); (c) majorly mesoporous (>90 % of the total pore volume), i.e., B875-LD-140h-Air, B875-LLD-280h-Air, B875-LD-140h-N_2, and B875-LLD-280h-N_2.

EDL behaviour of the selected electrodes was studied through CV analysis (Figures 8 and 9). According to the literature, an ideal EDL material has a rectangular-shaped voltammogram [30]. At the fastest sweep rate (i.e., 50 mV s^{-1}) the samples with the majorly microporous structure, i.e., group (a) electrodes, showed the highest deformation from rectangular shape (Figure 8). This can be attributed to the limited accessibility of ions to the micropores of activated biochar. Increasing the mesopore content, i.e., group (b) and (c) electrodes, resulted in improved voltammograms in terms of decreased deformation and consequently more rectangular shape at fast scanning rates. Nonetheless, as sweep rate reduced to 0.5-5 mV s^{-1}, all voltammograms showed minimal distortion from rectangular shape (Figure 9) most probably due to the longer time available for the ions to access the micropore content of the electrodes [45]. To measure the total capacitance of the electrodes, the anodic and cathodic current difference ($\Delta I=I_a - I_c$) at the EDL plateau region of the CV voltammograms was plotted against corresponding sweep rate (i.e., 0.5-3 mV s^{-1}). The slope of the plot was then quantified and normalized per mass of each electrode to calculate the total capacitance (F g^{-1}) (Table 3). Group (a) electrodes with

microporous structure (i.e., N_2-dried B675 samples) showed 10-20 % higher total capacitance values comparing to group (b) electrodes with mixed micro/meso-porous structure (i.e., B675-LD-140h-Air and B675-LLD-280h-Air). This could be attributed to the higher content of micropore volume in N_2-dried B675 samples vs. air-dried B675. According to the literature, micropores between 0.5-2 nm contribute to the electro-adsorption of simple hydrated ions (e.g., Na^+,OH^- and K^+), hence, increasing the total capacitance [46]. B875-LD-140h-Air and B875-LLD-280h-Air electrodes of group (c) (i.e., majorly mesoporous structure) showed total capacitance values comparable to B675-LD-140h-Air and B675-LLD-280h-Air electrodes with mixed micro/meso-porous structure (Table 3). The highest total capacitance was obtained for B875-LD-140h-N_2 (i.e., 95 % mesoporous structure) and B675-SD-15h-N_2 (i.e., 88 % microporous structure) electrodes, i.e., 240 and 245 F g^{-1}, respectively. Despite of almost identical total capacitance of these two electrodes, the B875-LD-140h-N_2 electrode showed more rectangular shape voltammogram indicative of its mesoporous structure and improved ion accessibility into the pores (Figure 8). The total capacitances of activated biochar electrodes with tailored porosity are competitive with promising carbon-based electrodes in the literature with high-cost and complicated preparation methods, e.g., modified carbon aerogel with Ru (206 F g^{-1}) [47], Graphene-PEDOT (Poly-ethylenedioxythiophene) (125-261 F g^{-1}) [48], Single wall carbon nanotubes on carbon cloth (190-210 F g^{-1}) [49], and AC from fibers of oil palm (150 F g^{-1}) [50].

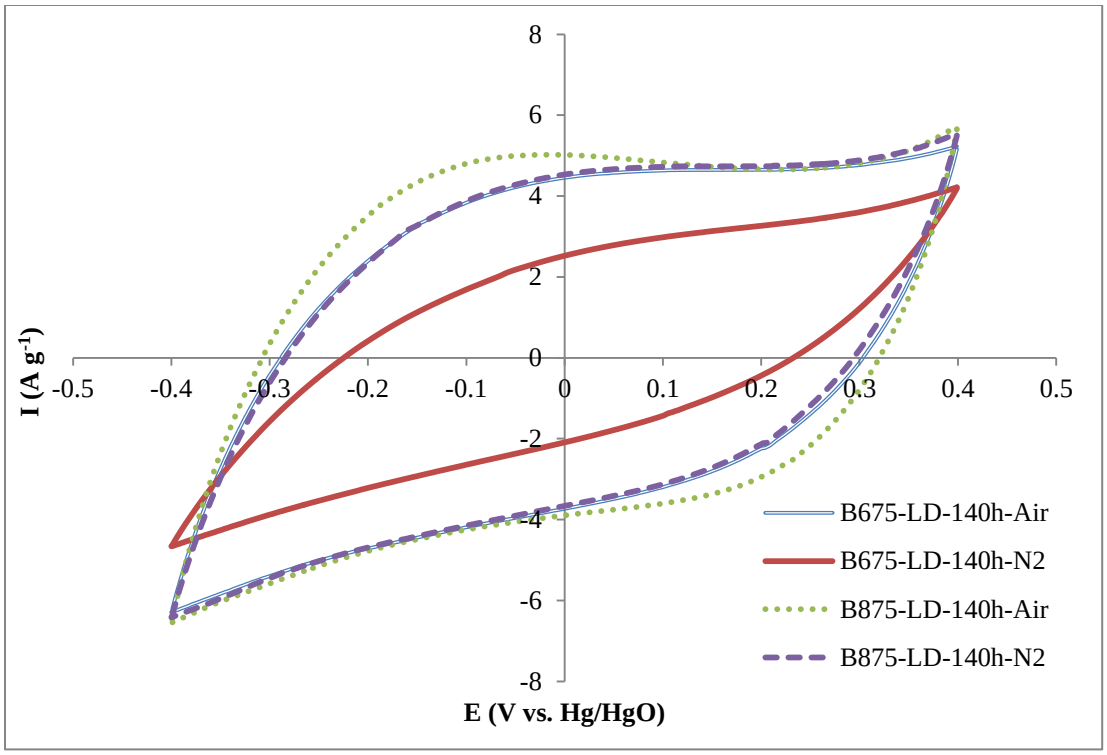

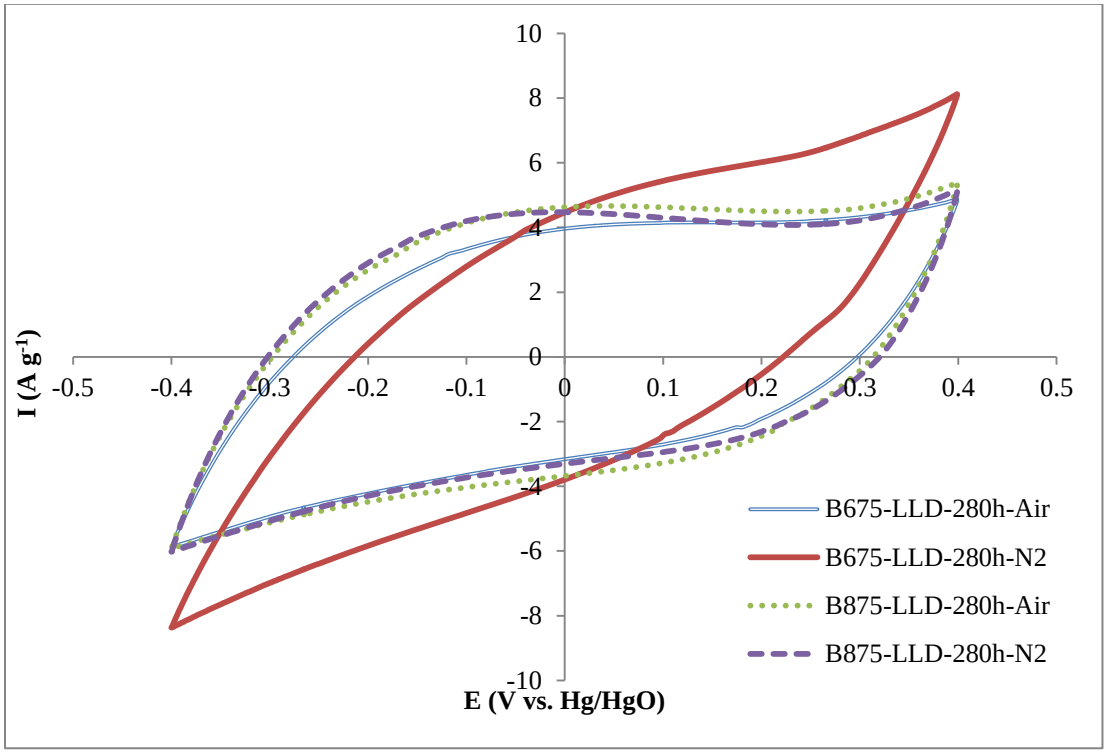

Figure 8. CV diagrams of tailored activated biochar electrodes at 50 mV s^{-1} in 0.1 mol L^{-1} NaCl/0.1 mol L^{-1} NaOH electrolyte.

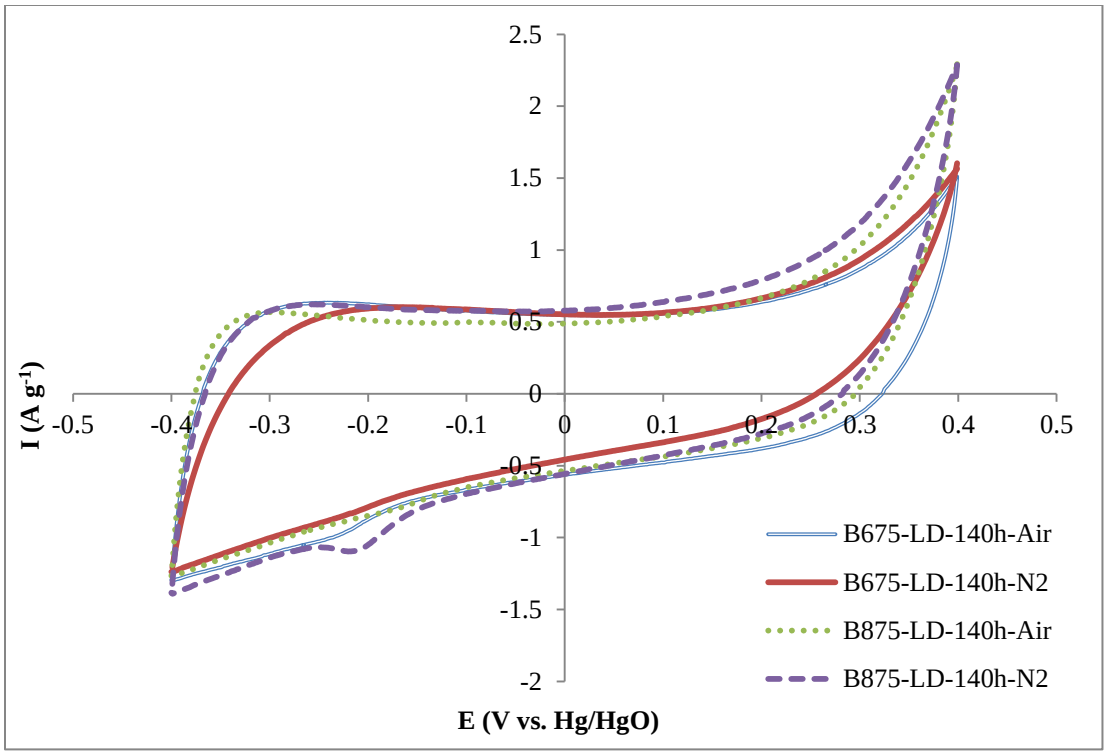

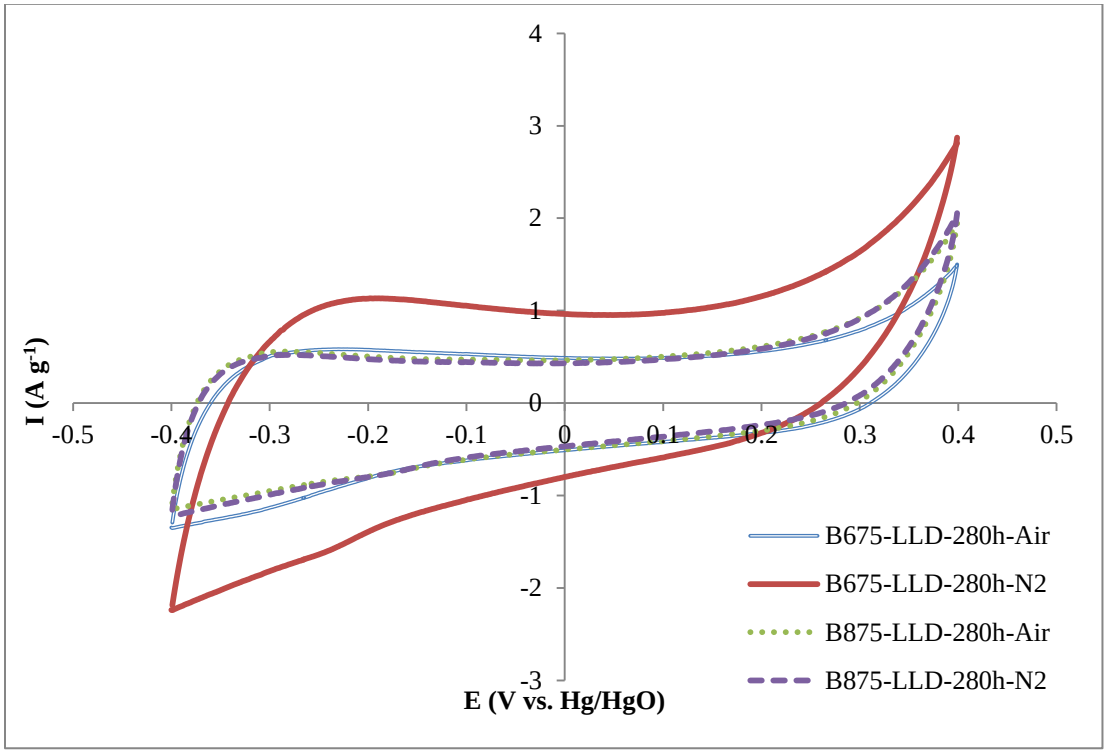

Figure 9. CV diagrams of tailored activated biochar electrodes at 5 mV s-1 in 0.1 mol L-1 NaCl/0.1 mol L-1 NaOH electrolyte.

Table 3. EDL capacitive properties of selected tailored activated biochar

Electrodes	Total capacitance ($F\ g^{-1}$)	Discharge capacitance ($F\ g^{-1}$)	Ohmic drop ($V\ g^{-1}$)	R_{ct} ($\Omega\ cm^{-2}$)	R_s ($\Omega\ cm^{-2}$)
Group (a)					
B675-SD-15h-N_2	245	55	0.71	0.203	0.108
B675-LD-140h-N_2	224	65	1.14	0.246	0.064
B675-LLD-280h-N_2	222	72	1.24	0.266	0.041
Group (b)					
B675-LD-140h-Air	212	62	0.62	0.154	0.052
B675-LLD-280h-Air	204	63	1.07	0.222	0.047
Group (c)					
B875-LD-140h-Air	218	58	0.33	0.114	0.026
B875-LLD-280h-Air	201	63	0.23	0.124	0.035
B875-LD-140h-N_2	240	82	0.22	0.063	0.032
B875-LLD-280h-N_2	182	55	0.29	0.092	0.026

The Galvanostatic Charge Discharge (GCD) tests were performed to further analyze the adsorption and desorption behaviour of ions from surface of electrodes. Figure 10 demonstrates the charge discharge profiles (at 2 and -2 mA, respectively) of selected activated biochar electrodes with tailored porosity. All GCD profiles showed typical triangle shape confirming the promising EDL behaviour of activated biochar. The sudden potential drop at the beginning of the discharge curve is known as Ohmic drop (i.e., iR drop) resulting from the total resistance of electrode majorly associated with electrical connection, bulk solution, and ion migration into pores [30,32]. The major difference in Ohmic drop of tailored electrodes is attributed to ion migration resistance into pores and the electrical conductivity (EC) of the activated biochar samples. Group (c) electrodes with >90 % mesoporosity showed the lowest Ohmic drop values; while, group (b) electrodes with the majority of microporous structure (i.e., N_2-dried B675 samples) showed the highest Ohmic drop (Table 3). These results suggest reduced electrode

resistance due to increased mesoporosity and consequently improved ion accessibility. The discharge capacitance was calculated by multiplying the slope of the linear portion of discharge diagram ($\Delta t/\Delta E$) with the amount of applied current (-2 mA) (Table 3). The highest discharge capacitance (i.e., 82 F g^{-1}) was obtained for B875-LD-140h-N_2 electrode with the highest mesoporosity content (95 %); where, the discharge capacitance of group (a) electrodes (with >88 % microporosity) ranged between 55-72 F g^{-1}. The discharge capacitance values obtained using tailored activated biochar are significantly larger than other carbon-based electrodes in the literature, e.g., commercial carbon aerogel (23 F g^{-1}), carbon black (10 F g^{-1}) and activated carbon (19 F g^{-1}) [51].

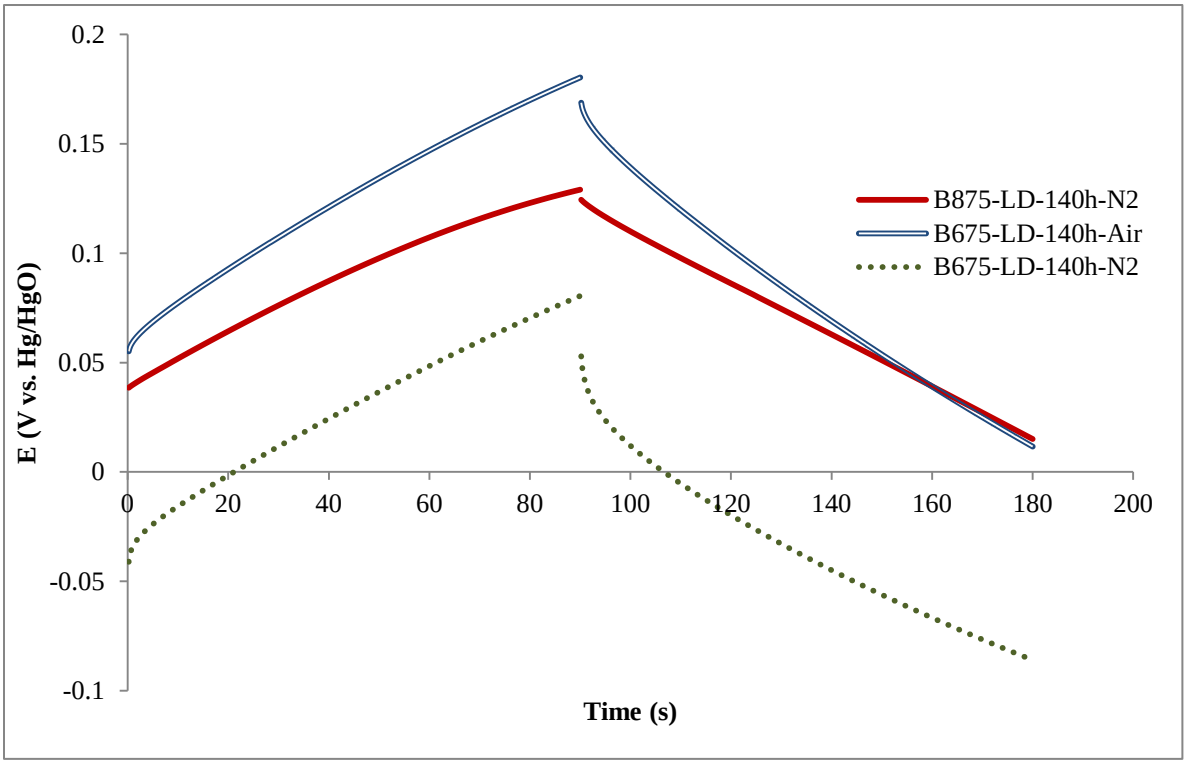

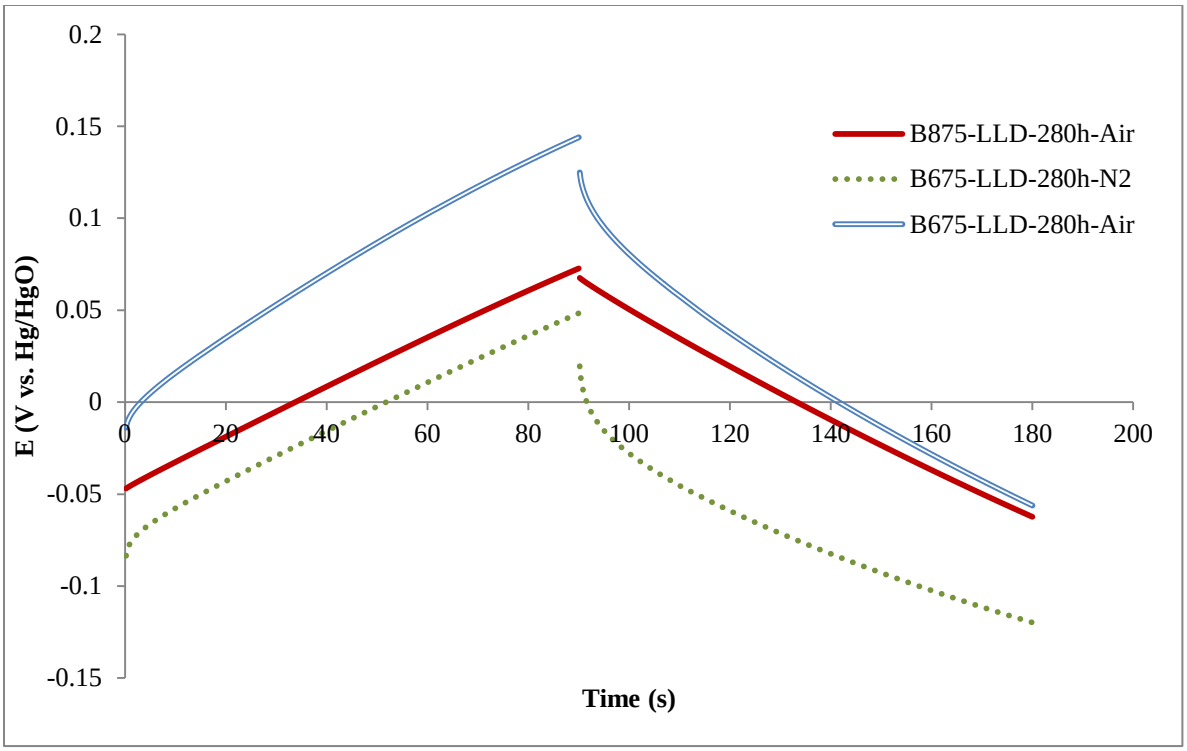

Figure 10. GCD plots of tailored activated biochar electrodes in 0.1 mol L^{-1} NaCl/0.1 mol L^{-1} NaOH electrolyte.

The tailored biochar electrodes were also characterized through Impedance Spectroscopy (EIS), with the Nyquist plots (i.e., complex impedance plots) shown in Figure 11. The typical Nyquist plot of an EDL capacitor includes a semi-circle at high frequencies, a mass transfer limited region shown by a linear line (Warburg region with ~45° phase angle), and a nearly vertical line at low frequencies (i.e., representative of ideal capacitive behaviour) [32,52,53]. The Nyquist plot of group (a) electrodes showed a depressed semi-circle at high frequencies followed by a linear region at low frequencies (i.e., diffusion-limited) mainly due to the high content of microporosity (Figure 11). Group (b) electrodes showed similar trend except for the steeper slope in the diffusion-limited region indicative of improved diffusion and better capacitive behaviour [32]. The activated biochar electrodes with majorly mesoporous structure showed perfect semi-

circle (inset of Figure 11) indicative of double layer performance followed by nearly vertical line confirming the ideal capacitive behaviour and minimal mass transfer limitations.

The intercept of semi-circle curve on the real part axis of impedance (Z') stands for the bulk solution resistance (R_s); while, the radius of the semi-circle represents the internal electrode resistance (R_{ct}, charge-transfer resistance). R_s is mainly dependant on the resistance associated with the solution and connectivity of particles to the current collector; where, R_{ct} is related to the ionic transfer resistance into the pores of electrode [32,54]. The Randles equivalent circuit was used to simulate the EIS data and quantify the values of R_s and R_{ct} (Table 3). As expected, the mesoporous electrodes of group (c) showed the lowest R_{ct} followed by group (b) electrodes with mixed micro/meso-porous structure and group (a) with microporous structure.

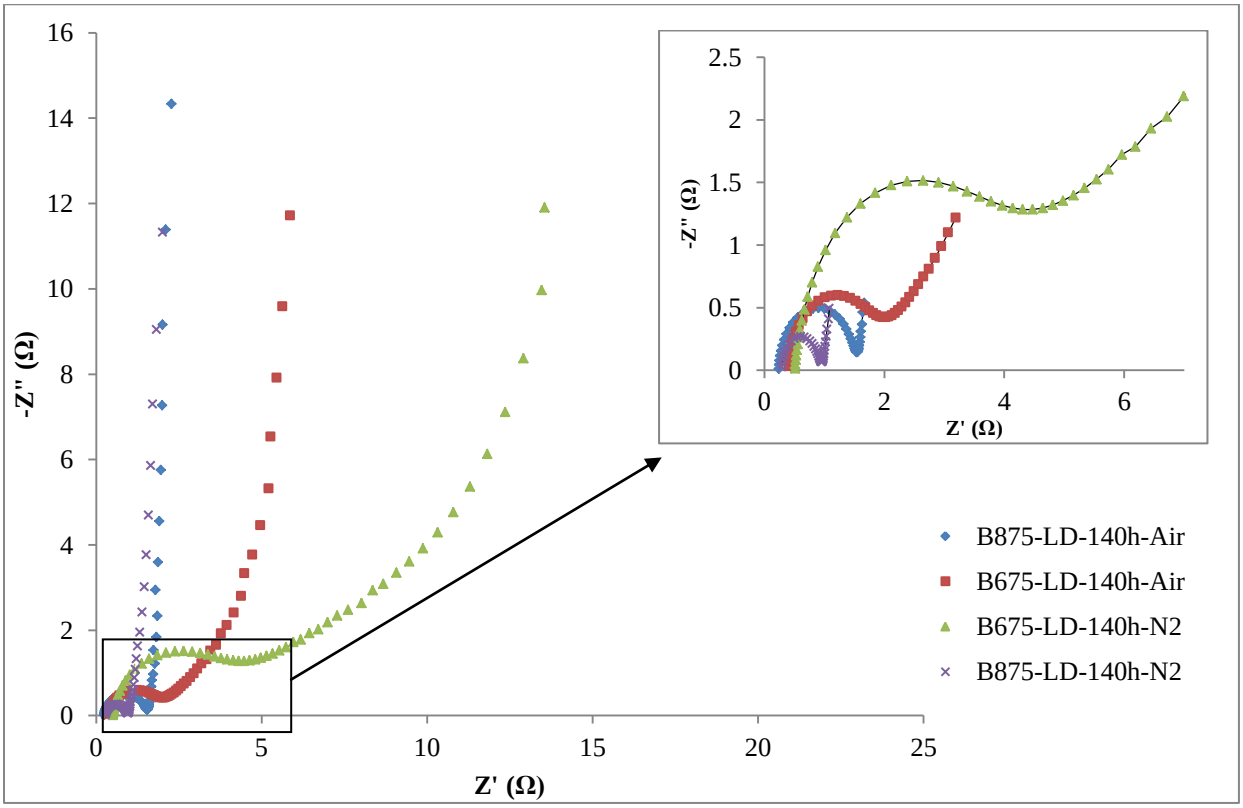

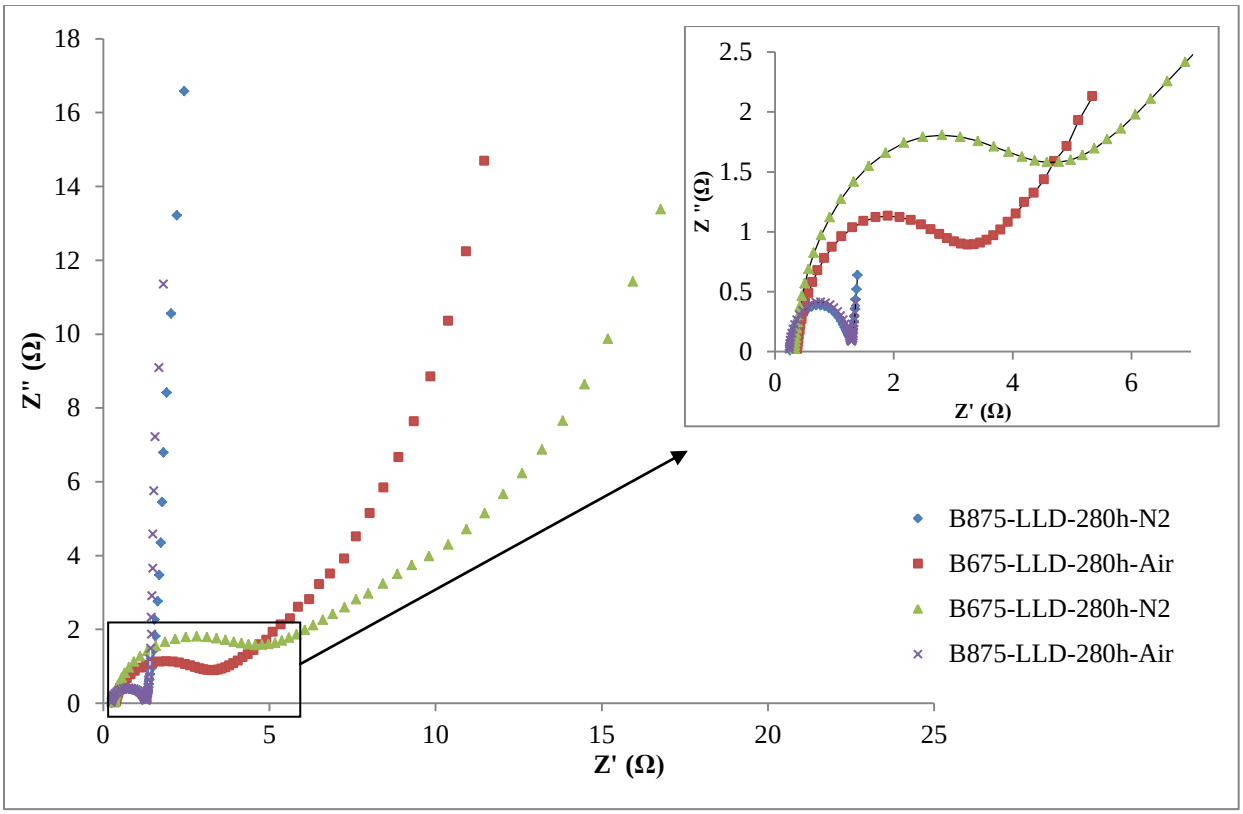

Figure 11. Nyquist plots of tailored activated biochar in 0.1 mol L^{-1} NaCl/0.1 mol L^{-1} NaOH electrolyte.

The Electrical Conductivity (EC) of powder activated biochar was also measured via dry-cell polarization experiment (Table 4). EC is one of the major characteristics of a promising double layer material affecting electrical connectivity and charge transfer within the electrode. The B475 samples (either N_2 or air dried) showed negligible EC (i.e., $>10^{-7}$ S cm^{-1}) which could be the main reason responsible for the poor EDL performance of the prepared electrodes despite of having large surface area and porosity (data not shown). Increasing the activation temperature to 675°C resulted in significantly improved EC (Table 4). Interestingly, further increase of EC was obtained for B875 samples with the mesoporous structure; while, EC is expected to be reduced by increasing porosity. The increased EC of the B675 and specifically B875 samples could be

attributed to the removal of heteroatom from the carbon matrix and increased electrons associated with π-bond as charge carriers [25,31].

Table 4. Electrical Conductivity of activated biochar powders

Sample	Electrical Conductivity (S cm^{-1} g^{-1})
B475-LD-Air	Negligible
B475-SD-N2	Negligible
B675-SD-N2	0.21
B675-LD-N2	0.037
B675-LLD-N2	0.043
B675-LD-Air	0.32
B675-LLD-Air	0.15
B875-LD-Air	2.10
B875-LLD-Air	1.03
B875-LD-N2	0.54
B875-LLD-N2	1.30

The EDL performance results of tailored biochar electrodes could suggest different range of potential applications from desalination of water with small hydrated ions (e.g., Na^+, Cl^-, Cu^{2+}, K^+, Mg^{2+}) using microporous electrodes to electrosorption of larger ions in industrial wastewater (e.g., Zn^{2+}, Cd^{3+}, Cr^{3+}) using mesoporous electrodes. Furthermore, microporous electrodes with high total capacitance can be potentially employed in supercapacitors using aqueous electrolytes (NaOH, KOH, H_2SO_4); while, mesoporous electrodes can be used in electrolytes with larger ionic radius (e.g., ionic liquids and aprotic electrolytes) to increase the energy density of the supercapacitor. These results confirm the potential practicality of activated biochar with tailored structure to improve the performance in an adsorption specific processe.

4. Conclusion

It was demonstrated for the first time that by modifying the drying conditions (drying gas and time) prior to carbonization at 475, 675, or 875°C, activated biochar samples with tailored porosity (microporous, mesoporous, or a combination of both) can be prepared. The KOH impregnated biochar was dried under air and N_2 for 0, 15, 140, and 280 h. The surface chemistry of air-dried and N_2-dried samples was analyzed via FTIR suggesting conversion of KOH to K_2CO_3 under air-drying particularly during prolonged drying; while, N_2-drying resulted in preservation of KOH independent of drying time. The effect of KOH to K_2CO_3 conversion as a result of drying conditions was found to have a significant effect on porosity development during carbonization at 475, 675 and 875°C. Air-dried samples carbonized at 475 and 675°C resulted in mixed micro- and meso-porous structures with a decreasing trend of surface area and micropore volume with increasing drying time. However, N_2-dried samples showed majorly microporous structure with comparable surface areas (i.e., <5 % difference) at 475 and 675°C independent of drying time. These results are attributed to the conversion of KOH to K_2CO_3 in the air-dried samples and preservation of KOH under N_2 drying condition. Increasing the carbonization temperature to 875°C using either air- or N_2-dried samples resulted in significantly high surface areas 2000-2672 m^2 g^{-1} with >90 % mesoporous structure. The implication of this finding is extremely important in adsorption, catalysis, electro-catalysis and electric double layer based applications requiring both high surface area and excellent mass transfer in the porous structure.

Application of activated biochar with tailored porosity was investigated in electric induced adsorption/desorption process for capacitive deionization of NaCl and potentially supercapacitor fabrication. Biochar electrodes with majorly microporous structure showed very high total capacitance (222-245 F g^{-1}) mainly due to their high content of micropores. However, the

increased capacitance was associated with hindered accessibility of ions to the pores resulting in larger electrode resistance as supported by Ohmic drop results. Increasing the mesopore content (to 40-50 % of the total pore volume) resulted in slightly reduced total capacitance (212 and 204 F g^{-1}, respectively) while decreasing the total resistance of electrodes compared to the microporous electrodes. Further increasing the mesopore content of the activated biochar (>90 % of the total pore volume) resulted in almost ideal capacitive behaviour with the smallest mass transfer limitation and electrode resistance as evidenced by impedance spectroscopy and galvanostatic charge/discharge studies. Total capacitance of mesoporous electrodes was in the range of 182-240 F g^{-1} depending on the drying conditions. These results confirm the utilization of activated biochar as a value-added renewable material in porosity-specific applications including but not limited to pollution abatement and energy storage.

Acknowledgment

The authors acknowledge the generous financial support of the Natural Sciences and Engineering Research Council of Canada (NSERC) Discovery and Discovery Accelerator Supplement grant program and Rio Tinto Alcan Canada Fund in the form of the Graduate Student Award to Amir Mehdi Dehkhoda.

References:

[1] Activated Carbon — Roskill http://www.roskill.com/reports/industrial-minerals/activated-carbon (accessed April 10, 2015).

[2] Song M, Jin B, Xiao R, Yang L, Wu Y, Zhong Z, et al. The comparison of two activation techniques to prepare activated carbon from corn cob. Biomass Bioenergy 2013;48:250–6. doi:10.1016/j.biombioe.2012.11.007.

[3] Titirici M-M. Sustainable Carbon Materials from Hydrothermal Processes. John Wiley & Sons; 2013.

[4] Lillo-Ródenas MA, Cazorla-Amorós D, Linares-Solano A. Understanding chemical reactions between carbons and NaOH and KOH: An insight into the chemical activation mechanism. Carbon 2003;41:267–75. doi:10.1016/S0008-6223(02)00279-8.

[5] Azargohar R, Dalai AK. Steam and KOH activation of biochar: Experimental and modeling studies. Microporous Mesoporous Mater 2008;110:413–21. doi:10.1016/j.micromeso.2007.06.047.

[6] Molina-Sabio M, Rodríguez-Reinoso F. Role of chemical activation in the development of carbon porosity. Colloids Surf Physicochem Eng Asp 2004;241:15–25. doi:10.1016/j.colsurfa.2004.04.007.

[7] Ahmadpour A, Do DD. The preparation of activated carbon from macadamia nutshell by chemical activation. Carbon 1997;35:1723–32. doi:10.1016/S0008-6223(97)00127-9.

[8] Hayashi J, Kazehaya A, Muroyama K, Watkinson AP. Preparation of activated carbon from lignin by chemical activation. Carbon 2000;38:1873–8. doi:10.1016/S0008-6223(00)00027-0.

[9] Tay T, Ucar S, Karagöz S. Preparation and characterization of activated carbon from waste biomass. J Hazard Mater 2009;165:481–5. doi:10.1016/j.jhazmat.2008.10.011.

[10] Lillo-Ródenas MA, Lozano-Castelló D, Cazorla-Amorós D, Linares-Solano A. Preparation of activated carbons from Spanish anthracite: II. Activation by NaOH. Carbon 2001;39:751–9. doi:10.1016/S0008-6223(00)00186-X.

[11] Lozano-Castelló D, Lillo-Ródenas MA, Cazorla-Amorós D, Linares-Solano A. Preparation of activated carbons from Spanish anthracite: I. Activation by KOH. Carbon 2001;39:741–9. doi:10.1016/S0008-6223(00)00185-8.

[12] Hayashi J, Horikawa T, Muroyama K, Gomes VG. Activated carbon from chickpea husk by chemical activation with K2CO3: preparation and characterization. Microporous Mesoporous Mater 2002;55:63–8. doi:10.1016/S1387-1811(02)00406-7.

[13] Robau-Sánchez A, Aguilar-Elguézabal A, Aguilar-Pliego J. Chemical activation of Quercus agrifolia char using KOH: Evidence of cyanide presence. Microporous Mesoporous Mater 2005;85:331–9. doi:10.1016/j.micromeso.2005.07.003.

[14] Sudaryanto Y, Hartono SB, Irawaty W, Hindarso H, Ismadji S. High surface area activated carbon prepared from cassava peel by chemical activation. Bioresour Technol 2006;97:734–9. doi:10.1016/j.biortech.2005.04.029.

[15] Hayashi J, Horikawa T, Takeda I, Muroyama K, Nasir Ani F. Preparing activated carbon from various nutshells by chemical activation with K2CO3. Carbon 2002;40:2381–6. doi:10.1016/S0008-6223(02)00118-5.

[16] Adinata D, Wan Daud WMA, Aroua MK. Preparation and characterization of activated carbon from palm shell by chemical activation with K2CO3. Bioresour Technol 2007;98:145–9. doi:10.1016/j.biortech.2005.11.006.

[17] Deng H, Li G, Yang H, Tang J, Tang J. Preparation of activated carbons from cotton stalk by microwave assisted KOH and K2CO3 activation. Chem Eng J 2010;163:373–81. doi:10.1016/j.cej.2010.08.019.

[18] Avraham E, Yaniv B, Soffer A, Aurbach D. Developing Ion Electroadsorption Stereoselectivity, by Pore Size Adjustment with Chemical Vapor Deposition onto Active Carbon Fiber Electrodes. Case of Ca2+/Na+ Separation in Water Capacitive Desalination. J Phys Chem C 2008;112:7385–9. doi:10.1021/jp711706z.

[19] Pang J, Hu Q, Wu Z, Eric Hampsey J, He J, Lu Y. Direct synthesis of unimodal and bimodal nanoporous carbon. Microporous Mesoporous Mater 2004;74:73–8. doi:10.1016/j.micromeso.2004.06.009.
[20] Baccar R, Bouzid J, Feki M, Montiel A. Preparation of activated carbon from Tunisian olive-waste cakes and its application for adsorption of heavy metal ions. J Hazard Mater 2009;162:1522–9. doi:10.1016/j.jhazmat.2008.06.041.
[21] Amuda OS, Giwa AA, Bello IA. Removal of heavy metal from industrial wastewater using modified activated coconut shell carbon. Biochem Eng J 2007;36:174–81. doi:10.1016/j.bej.2007.02.013.
[22] Lehmann J, Joseph S. Biochar for Environmental Management: Science and Technology. Earthscan Publications Ltd.; 2009.
[23] Laird DA, Brown RC, Amonette JE, Lehmann J. Review of the pyrolysis platform for coproducing bio-oil and biochar. Biofuels Bioprod Biorefining 2009;3:547–62. doi:10.1002/bbb.169.
[24] Woolf D, Amonette JE, Street-Perrott FA, Lehmann J, Joseph S. Sustainable biochar to mitigate global climate change. Nat Commun 2010;1:56. doi:10.1038/ncomms1053.
[25] Dehkhoda AM, Ellis N, Gyenge E. Electrosorption on activated biochar: effect of thermo-chemical activation treatment on the electric double layer capacitance. J Appl Electrochem 2014;44:141–57. doi:10.1007/s10800-013-0616-4.
[26] Mohan D, Sarswat A, Ok YS, Pittman Jr. CU. Organic and inorganic contaminants removal from water with biochar, a renewable, low cost and sustainable adsorbent – A critical review. Bioresour Technol n.d. doi:10.1016/j.biortech.2014.01.120.
[27] Oren Y. Capacitive deionization (CDI) for desalination and water treatment -- past, present and future (a review). Desalination 2008;228:10–29. doi:10.1016/j.desal.2007.08.005.
[28] Welgemoed TJ, Schutte CF. Capacitive Deionization Technology™: An alternative desalination solution. Desalination 2005;183:327–40. doi:10.1016/j.desal.2005.02.054.
[29] Anderson MA, Cudero AL, Palma J. Capacitive deionization as an electrochemical means of saving energy and delivering clean water. Comparison to present desalination practices: Will it compete? Electrochimica Acta 2010;55:3845–56. doi:10.1016/j.electacta.2010.02.012.
[30] Frackowiak E, Béguin F. Carbon materials for the electrochemical storage of energy in capacitors. Carbon 2001;39:937–50. doi:10.1016/S0008-6223(00)00183-4.
[31] Pandolfo AG, Hollenkamp AF. Carbon properties and their role in supercapacitors. J Power Sources 2006;157:11–27. doi:16/j.jpowsour.2006.02.065.
[32] Ghosh A, Lee YH. Carbon-Based Electrochemical Capacitors. ChemSusChem 2012;5:480–99. doi:10.1002/cssc.201100645.
[33] Settle FA. Handbook of Instrumental Techniques for Analytical Chemistry. Englewood CLiffs, NJ: Prentice Hall; 1997.
[34] Brewer CE, Schmidt-Rohr K, Satrio JA, Brown RC. Characterization of biochar from fast pyrolysis and gasification systems. Environ Prog Sustain Energy 2009;28:386–96. doi:10.1002/ep.10378.
[35] Urabe Y, Ishikura T, Kaneko K. Development of porosity in carbons from yeast grains by activation with alkali metal carbonates. J Colloid Interface Sci 2008;319:381–3. doi:10.1016/j.jcis.2007.10.057.
[36] Guo J, Lua AC. Textural and Chemical Characterizations of Adsorbent Prepared from Palm Shell by Potassium Hydroxide Impregnation at Different Stages. J Colloid Interface Sci 2002;254:227–33. doi:10.1006/jcis.2002.8587.
[37] Raymundo-Piñero E, Azaïs P, Cacciaguerra T, Cazorla-Amorós D, Linares-Solano A, Béguin F. KOH and NaOH activation mechanisms of multiwalled carbon nanotubes with different structural organisation. Carbon 2005;43:786–95. doi:10.1016/j.carbon.2004.11.005.
[38] Franklin RE. Crystallite growth in graphitizing and non-graphitizing carbons. Proc R Soc Lond Ser Math Phys Sci 1951:196–218.
[39] Technology TEP of CTI of, Binghamton MSP of PU of NY at, University MEP of EES. Graphite Intercalation Compounds and Applications. Oxford University Press; 2003.

[40] McKee DW. Gasification of graphite in carbon dioxide and water vapor—the catalytic effects of alkali metal salts. Carbon 1982;20:59–66. doi:10.1016/0008-6223(82)90075-6.
[41] Morishige K, Tarui N. Capillary Condensation of Nitrogen in Ordered Mesoporous Silica with Bicontinuous Gyroid Structure. J Phys Chem C 2006;111:280–5. doi:10.1021/jp064946s.
[42] Thommes M. Physical Adsorption Characterization of Nanoporous Materials. Chem Ing Tech 2010;82:1059–73. doi:10.1002/cite.201000064.
[43] Lowell S. Characterization of Porous Solids and Powders: Surface Area, Pore Size and Density. Springer Science & Business Media; 2004.
[44] Rouquerol J, Rouquerol F, Llewellyn P, Maurin G, Sing KSW. Adsorption by Powders and Porous Solids: Principles, Methodology and Applications. Academic Press; 2013.
[45] Panić VV, Stevanović RM, Jovanović VM, Dekanski AB. Electrochemical and capacitive properties of thin-layer carbon black electrodes. J Power Sources 2008;181:186–92. doi:10.1016/j.jpowsour.2008.03.048.
[46] Qu D, Shi H. Studies of activated carbons used in double-layer capacitors. J Power Sources 1998;74:99–107. doi:10.1016/S0378-7753(98)00038-X.
[47] Miller JM, Dunn B, Tran TD, Pekala RW. Deposition of Ruthenium Nanoparticles on Carbon Aerogels for High Energy Density Supercapacitor Electrodes. J Electrochem Soc 1997;144:L309–11. doi:10.1149/1.1838142.
[48] Alvi F, Ram MK, Basnayaka PA, Stefanakos E, Goswami Y, Kumar A. Graphene–polyethylenedioxythiophene conducting polymer nanocomposite based supercapacitor. Electrochimica Acta 2011;56:9406–12. doi:10.1016/j.electacta.2011.08.024.
[49] Hsu Y-K, Chen Y-C, Lin Y-G, Chen L-C, Chen K-H. High-cell-voltage supercapacitor of carbon nanotube/carbon cloth operating in neutral aqueous solution. J Mater Chem 2012;22:3383. doi:10.1039/c1jm14716a.
[50] Farma R, Deraman M, Awitdrus A, Talib IA, Taer E, Basri NH, et al. Preparation of highly porous binderless activated carbon electrodes from fibres of oil palm empty fruit bunches for application in supercapacitors. Bioresour Technol 2013;132:254–61. doi:10.1016/j.biortech.2013.01.044.
[51] Zhao Y, Zheng M, Cao J, Ke X, Liu J, Chen Y, et al. Easy synthesis of ordered meso/macroporous carbon monolith for use as electrode in electrochemical capacitors. Mater Lett 2008;62:548–51. doi:16/j.matlet.2007.06.002.
[52] Dolah BNM, Othman M a. R, Deraman M, Basri NH, Farma R, Talib IA, et al. Supercapacitor Electrodes from Activated Carbon Monoliths and Carbon Nanotubes. J Phys Conf Ser 2013;431:012015. doi:10.1088/1742-6596/431/1/012015.
[53] Wu C, Wang X, Ju B, Bai Y, Jiang L, Wu H, et al. Supercapacitive behaviors of the nitrogen-enriched activated mesocarbon microbead in aqueous electrolytes. J Solid State Electrochem 2013;17:1693–700. doi:10.1007/s10008-013-2038-y.
[54] Taer E, Deraman M, Talib IA, Hashmi SA, Umar AA. Growth of platinum nanoparticles on stainless steel 316L current collectors to improve carbon-based supercapacitor performance. Electrochimica Acta 2011;56:10217–22. doi:10.1016/j.electacta.2011.09.007.